Directional multiscale representations and applications in digital neuron reconstruction

Cihan Kayasandik[b], Kanghui Guo[a], Demetrio Labate[b,*]

[a] *Missouri State University, Department of Mathematics, Springfield, Missouri, USA*
[b] *University of Houston, Department of Mathematics, Houston, Texas, USA*
[c] *University of Texas Medical Branch, Department of Pharmacology and Toxicology, Galveston, Texas, USA*

Abstract

Recent advances in the field of multiscale representations have introduced a new generation of powerful techniques with great potential for the analysis of images and other multidimensional data. These novel techniques enable the quantification of essential geometric characteristics in complex imaging data resulting in improved algorithms for images denoising, feature extraction and classification. In this paper, we present selected applications of these ideas to problems of neuroscience imaging with special attention to the problem of digital neuron reconstruction.

Keywords: fluorescent microscopy, multiscale analysis, neuron profiling, neuron reconstruction, sparse representations, wavelets

2010 MSC: 42C15, 42C40, 92C15, 92C55

1. Introduction

Remarkable advances in fluorescent microscopy during the last decade have created great opportunities for scientific investigation and discovery in neuroscience by enabling fast acquisition of large volumes of high-resolution images. However, to process such data efficiently and take advantage of the wealth of information made available by new technologies, there is not only a need of

*Corresponding author
Email addresses: kayasa89@math.uh.edu (Cihan Kayasandik), KanghuiGuo@MissouriState.edu (Kanghui Guo), dlabate@math.uh.edu (Demetrio Labate)

improved and highly specialized image processing algorithms but also of more targeted and conceptually innovative strategies to interrogate the data.

To address such challenges, a major interdisciplinary effort is being undertaken by the scientific community that brings together ideas from mathematics, statistics and computer science. As a result of this effort, several remarkable initiatives were launched in recent years aimed at tackling specific image processing tasks in the field of neuroscience, including neuron segmentation, cell counting and most prominently digital neuron reconstruction [1, 2, 3, 4, 5]. Digital neuron reconstruction or neuronal tracing requires to automatically reconstruct neuronal morphology in an image by recovering the graph connectivity of the neuronal processes and other shape characteristics (e.g., neurite length, neurite diameter). By tracing neurons and extracting their fundamental morphometric characteristics, researchers can understand neuronal structure and investigate fundamental relationships between shape properties and neuronal function. Due to the high complexity of neuron morphology and the low signal-to-noise ratio found in many images however, digital neuron reconstruction is among the most difficult tasks in computational neuroscience [6]. Despite the progress made in recent years, significant challenges remain to be solved.

In this paper, we illustrate the impact of emerging ideas from the area of multiscale analysis to applications in neuroscience imaging, with particular attention to problems of segmentation and feature extraction that are relevant in digital neuron reconstruction. By combining multiscale analysis and directional sensitivity, directional multiscale methods can be more effective than conventional methods in extracting critical information from images containing complex structures. The excellent performance of these methods when applied to image denoising and enhancement has been already demonstrated in the literature. One novel contribution of this paper is the application of these ideas to detect morphological properties of neurons through a geometric descriptor called Directional Ratio. We provide a novel theoretical analysis to show that this method precisely quantifies the degree of local anisotropy of indicator functions of planar regions and that this property can be applied to reliably separate

neuronal sub-compartments in microscopy images. We also discuss how this method for neuronal segmentation is combined with other ideas to design an innovative algorithm for neuronal tracing.

The rest of the paper is organized as follows. In Sec. 2, we review the application of advanced multiscale representations to image denoising. In Sec. 3, we analyze the properties of the Directional Ratio and illustrate its application for the separation of somas and dendrites in fluorescent images of neurons. In Sec. 4, we discuss how our method for the separation of somas and dendrites is applied to designed an improved algorithm for neuron sorting and tracing.

2. Image preprocessing

In order to take best advantage of instrumentation and remove unwanted artifacts, image acquired using fluorescent microscopy are typically preprocessed to remove noise and blur or to enhance specific features in preparation of further processing. Edges in particular play a prominent role in biomedical images as they separate organs and other structures of interest. Unfortunately, standard approaches to image restoration, e.g., median filtering and low-pass filtering, but also conventional wavelet thresholding may perform poorly especially in very noisy situations. By contrast, schemes based on advanced multiscale representations such as curvelets and shearlets lead to generally better performing algorithms due to their ability to preserve edge information.

2.1. Shearlets and curvelets

Shearlets and curvelets were introduced during the last decade as refinements of conventional wavelets with the aim to overcome the limitations of traditional multiscale systems in dealing with multidimensional data [7, 8, 9]. Both methods consist of systems of well-localized waveforms defined not only over a range of scales and locations, like wavelets, but also over multiple orientations and with highly anisotropic shapes. Due to their high directional sensitivity, they are especially efficient to approximate edges and other elongated features in images.

In dimension $n = 2$, shearlets are generated by the action of anisotropic dilations and shear transformations on a pair of generator functions $\psi^{(\nu)} \in L^2(\mathbb{R}^2)$, $\nu = 1, 2$, that is,

$$\psi^{(\nu)}_{j,\ell,k}(x) = 2^{3j/2}\psi^{(\nu)}(B^{\ell}_{\nu}A^{j}_{\nu}x - k), \tag{1}$$

for $j \geq 0$, $-2^j \leq \ell \leq 2^j$, $k \in \mathbb{Z}^2$, where $A_1 = \left(\begin{smallmatrix} 4 & 0 \\ 0 & 2 \end{smallmatrix}\right), A_2 = \left(\begin{smallmatrix} 2 & 0 \\ 0 & 4 \end{smallmatrix}\right)$ are the *anisotropic dilation matrices* and $B_1 = \left(\begin{smallmatrix} 1 & 1 \\ 0 & 1 \end{smallmatrix}\right)$, $B_2 = B_1^t$ are the *shear matrices*. Hence the indices j, ℓ, k are associated with a range of scales, orientations and locations, respectively.

By appropriately choosing the generators and adding an appropriate coarse scale system $\widetilde{\psi}_{-1,k} = \phi(\cdot - k)$, $k \in \mathbb{Z}^2$, (see [10] for details), one obtains a smooth Parseval frame of shearlets for $L^2(\mathbb{R}^2)$. With compact notation, we denote this system as

$$\{\widetilde{\psi}_{\mu},\ \mu \in M\}, \tag{2}$$

where $\widetilde{\psi}_{j,\ell,k,\nu} = \psi^{(\nu)}_{j,\ell,k}$ and $M = M_C \cup M_F$ are the indices associated with coarse-scale and fine-scale shearlets, respectively; that is, $M_C = \{(j,k) : j = -1, k \in \mathbb{Z}^2\}$, $M_F = \{(j,\ell,k,\nu) : j \geq 0, |\ell| < 2^j, k \in \mathbb{Z}^2, \nu = 1, 2)\}$. We have the following result from [10]:

Theorem 1. *The system of shearlets* (2) *is a Parseval frame for* $L^2(\mathbb{R}^2)$. *That is, for any* $f \in L^2(\mathbb{R}^2)$, *we have the reproducing formula*

$$f = \sum_{\mu \in M} \langle f, \widetilde{\psi}_{\mu} \rangle\, \widetilde{\psi}_{\mu}, \tag{3}$$

with convergence in the L^2*-norm. All elements* $\{\widetilde{\psi}_{\mu},\ \mu \in M\}$ *are* C^{∞} *and compactly supported in the Fourier domain.*

Curvelets have a different and slightly more involved construction that involves anisotropic dilations, rotations and (non-integer) translations. Also in this case, one obtains a Parseval frame of $L^2(\mathbb{R}^2)$ [7].

By combining multiscale analysis and high directional sensitivity, shearlets and curvelets provide highly sparse representations for a large class of multi-

dimensional data, outperforming conventional wavelets. The superior approximation properties of these methods is well illustrated by considering the class of *cartoon-like* functions, a function space that is frequently used to model an idealized class of images with edges. Roughly speaking, this space consists of functions that are C^2 regular away from C^2 edges [11]. One can prove that shearlets or curvelets provide (nearly) optimally sparse approximations in the class of carton-like functions [11].

Theorem 2. *Let $f \in E^2$, the class of carton-like functions in $\mathbb{R}^2$, and f_N be its N-term approximation obtained by taking the N largest coefficients in the shearlet representation of f. Then:*

$$\|f - f_N\|_2^2 \leq C\, N^{-2} (\log N)^3. \tag{4}$$

Curvelets achieve the same type of approximation rate [7].

Ignoring the log factor, this result yields the optimal decay rate (no other basis or frame can achieve faster decay rate than N^{-2}). By contrast, wavelet approximations produce an error rate that is of order N^{-1}.

2.2. Image denoising

A classical implication of sparsity is statistical estimation.

Consider the problem of recovering an image f from noisy observations. We adopt the assumption that the image f to be recovered is a cartoon-like image and that the noise is additive white noise with level σ, that is, we observe $y = f + n$ where n is a Gaussian random process with zero mean and standard deviation σ. It then follows from the sparse approximation result that a standard image restoration strategy based on the shrinkage of representation coefficients yields an estimator $\tilde{f}$ whose Mean Squared Error (MSE) obeys (ignoring log-like factors)

$$\sup_{f \in F} E\|f - \tilde{f}\|^2 \asymp \sigma^{4/3}, \quad \text{as } \sigma \to 0.$$

This is the optimal rate of convergence as the minimax rate scales like $\sigma^{4/3}$. There are no other estimating procedure which gives better MSEs in an asymptotic sense [7, 11]. Note that, since the wavelet approximation rate is lower,

then wavelet shrinkage methods only achieve a MSE which scales like σ asymptotically as $\sigma \to 0$.

3. Soma segmentation

Even though there are several types of specialized neurons, each cell typically consists of a cell body or *soma*, several processes called *dendrites* and one long and thin process called *axon*. The term *neurite* is used to refer to either a dendrite or an axon.

In many applications, it is important to accurately detect and segment neuronal sub-compartments. However, to carry over such tasks automatically can be challenging due to the lack of selective markers and the large variability in shape and size of such structures. In fluorescent images of neuronal cultures, somas are usually visualized in the channel marked by the MAP2 (microtubules associated protein 2) antibody staining which is diffusely distributed in somas and dendrites. It is also possible to use a marker to visualized the cell nucleus but this organ occupies only a relatively small region inside the soma. In any case, further processing is needed to separate somas from neurites.

The simplest method for separating the two structures is to threshold the image based on local intensity values [12, 13]. However this approach performs rather poorly since high-intensity regions are frequently found outside somas. Algorithms based on morphological operators perform significantly better but are very sensitive to parameter setting (e.g., size of structuring elements) and require significant manual intervention to perform reliably [14, 15]. Performance of these methods may decrease significantly when images contain multiple cells and somas are clustered together [16]. To overcome existing limitations in problems of soma detection and segmentation, the authors of this paper have recently introduced a new geometric descriptor called Directional Ratio that relies on the geometric notion of *local isotropy* [17].

Definition 1. *A point x in a region A is a point of isotropy of A at scale s if there is a ball of radius $s/2$ centered at x which is entirely contained in A.*

Intuitively, in an image containing both blob-like and vessel-like regions, we expect to find a range of scales such that the points inside the blob-like regions are points of local isotropy whereas this is not true for the points inside the vessels. Hence, we can discriminate somas from neurites by finding regions of local isotropy over an appropriate range of scales.

3.1. Directional Ratio and soma detection

The Directional Ratio was introduced as an algorithmic and practical method to identify points in an image based on local isotropy properties [18]. For that, we need to consider a collection of *multiscale directional filters*, that is, an appropriate set of functions $\{\phi_{a,\theta} : a > 0, \theta \in [0, \pi)\} \subset L^2(\mathbb{R}^2)$, where a is a scale parameter and θ is a directional parameter. Hence the *Directional Ratio of a function* $f \in L^2(\mathbb{R}^2)$ *at scale* a *and location* $p \in \mathbb{R}^2$ is given by

$$D_a f(p) = \frac{\min_{\theta\in[0,\pi)}\{|f * \phi_{a,\theta}(p)|\}}{\max_{\theta\in[0,\pi)}\{|f * \phi_{a,\theta}(p)|\}}. \tag{5}$$

$D_a f(p)$ quantifies the degree of isotropy of f at location p and scale a by comparing the smallest directional filter response vs the largest one. If the filter response is independent of the direction, then $D_a f(p) = 1$ and this indicates that p is a point of local isotropy of f at scale a. Values $D_a f(p) < 1$ describe the degree of anisotropy of f at p at scale a.

A very simple choice of filters consists in choosing rotated and rescaled versions of a rectangular window. That is, we set $\phi = \chi_Q$, where Q is the rectangle $[-L/2, L/2] \times [-1/2, 1/2]$, for a fixed parameter $L \geq 1$. Next we define the *multiscale directional rectangular filters* $\phi_{a,\theta} = D_a R_\theta \phi$, where R_θ denotes the 2D rotation by an angle $(-\theta)$ and D_a is the (anisotropic) dilation operator $D_a f(x_1, x_2) = a^{-\frac{1+\alpha}{2}} f(a^{-1}a_1, a^{-\alpha}x_2)$, for a fixed $\alpha \in (0, 1]$; the parameter α controls the anisotropy of the scaling being applied (no anisotropy for $\alpha = 1$, increasingly more anisotropy as α approaches 0). Hence, the filters $\phi_{a,\theta}$ are indicator functions of oriented rectangular windows $Q_{a,\theta}$ obtained by rescaling Q by a along the x direction and by a^α along the y direction, and next rotating the resulting rectangle by θ.

To assess the theoretical performance of the Directional Ratio for separating regions of different local isotropy, we examine below its application to the characteristic of a disk and a long and thin rectangle. This function is meant to be a highly idealized model of the image of a cell body and a vessel. In practice, cell bodies found in experimental images can be rather elongated and vessels are usually not straight. However, we will show that the predictions of the theorem hold remarkably well in more realistic images.

Theorem 3. *Let $f = \chi_{S \cup N}$ where S is a disk of radius $R > 0$ and N is a rectangle of infinite length and width w, where $S \cap N = \varnothing$. Let the Directional Ratio be given by* (5) *with the multiscale directional rectangular filters $\phi_{a,\theta}$ defined as above.*

(a) Assume $L \geq 2w$. Then, for any $p \in N$, provided that $a > 4w/L$ and $a^{1-\alpha} > 4/L$, it follows that $D_a f(p) < 1/2$.

(b) There exists a range of scales such that for all points p inside the disk of radius $0.65R$ concentric with S we have $D_a f(p) > 1/2$.

PROOF. (a) Without loss of generality, suppose that N is centered at the origin, with the long axis parallel to the y coordinate. We start by observing that

$$D_a f(p) \leq \frac{|f * \phi_{a,0}(p)|}{|f * \phi_{a,\pi/2}(p)|}.$$

We consider first the case $\theta = 0$, where the rectangle $Q_{a,0}$ associated with the filter $\phi_{a,0}$ is horizontal. In this case, since $L \geq 2w$, the convolution is the same for any $p \in N$; hence, $f * \phi_{a,0}(p) = a^{-\frac{1+\alpha}{2}} w a^{\alpha}$. When $\theta = \pi/2$, the convolution depends on the value of the x coordinate of p. Its value is minimized when $p = (w/2, y)$ (i.e., p at the boundary of N), in which case $f * \phi_{a,\pi/2}(p) = a^{-\frac{1+\alpha}{2}} \frac{a^{\alpha}}{2} aL$. If $a^{\alpha} \leq w$ (width of filter less or equal than w), using the assumption that $a > 4w/L$, it follows that, for any $p \in N$

$$D_a f(p) \leq \frac{a^{-\frac{1+\alpha}{2}} w a^{\alpha}}{a^{-\frac{1+\alpha}{2}} \frac{a^{\alpha}}{2} aL} = \frac{2w}{aL} < \frac{1}{2}.$$

Otherwise, if $a^{\alpha} > w$ (width of filter larger than w), $f * \phi_{a,\pi/2}(p) \geq a^{-\frac{1+\alpha}{2}} \frac{w}{2} aL$

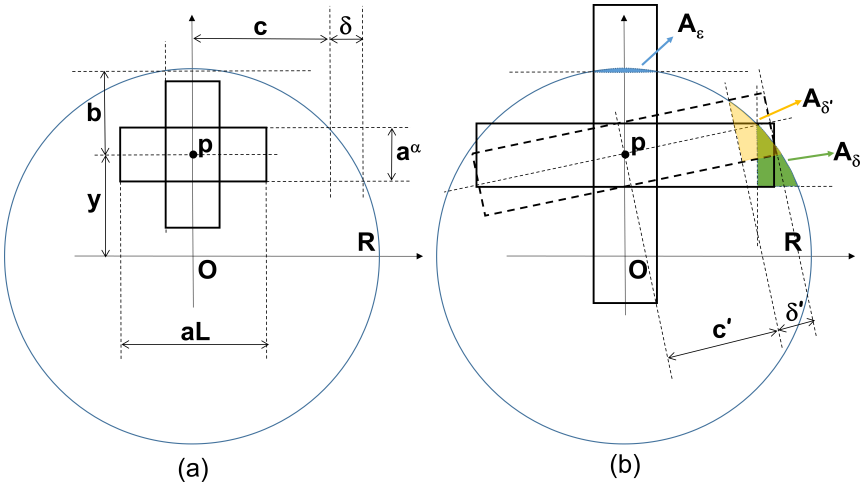

Figure 1: Computation of the Directional Ratio of the characteristic function of a disk of radius R and center O at $p = (0, y)$. (a) At small scales, when $\frac{aL}{2} \leq b$ (case 1 in narrative), any oriented rectangle $Q_{a,\theta}$ is contained inside the disk (here we show two rectangles at scale a and orientations $\theta = 0, \pi/2$). (b) At larger scales, $c < \frac{aL}{2} \leq 2c - b$ (case 3 in narrative), the area of the region of overlap of the disk and $Q_{a,\theta}$ depends on θ.

so that, using the assumption that $a^{1-\alpha} > 4/L$, we have

$$D_a f(p) \leq \frac{a^{-\frac{1+\alpha}{2}} w a^\alpha}{a^{-\frac{1+\alpha}{2}} \frac{w}{2} aL} = \frac{2a^\alpha}{aL} < \frac{1}{2}.$$

(b) Without loss of generality, let us assume that S is centered at the origin and p is located on the vertical axis, i.e., $p = (0, y)$, $0 \leq y \leq 0.65R$. Also, let us assume $a^\alpha \leq \frac{1}{5}R$.

If p is at the origin, i.e., $y = 0$, then $f * \phi_{a,\theta}(p)$ is independent of θ and hence $D_a f(p) = 1$. If p is not at the origin, then let b and c be given as in Fig. 1(a); that is, they denote the half-length of the longest vertical and horizontal rectangles, respectively, centered ap P and fully contained inside the disk. We discuss below several cases. Note that, since $y \leq 0.65R$ and $R > 5a^\alpha$, it follows that $b > a^\alpha$.

Case 1. $\frac{aL}{2} \leq b$. Note that $b \leq c$. Hence the rectangles $Q_{a,\theta}$ of length L centered at p are fully contained inside S for all orientations θ and $D_a f(p) = 1$.

Case 2. $b < \frac{aL}{2} \leq c$. Since $b \leq c$, the filter response $|f * \phi_{a,\theta}(p)|$ is maximal

when $\theta = 0$ and minimal when $\theta = \pi/2$. We denote by A_ϵ the area of region of intersection of the rectangle $Q_{a,\pi/2}$ and the disk S for $y > b$ (see Fig. 1(b)). Hence

$$D_a f(p) = \frac{(b + \frac{aL}{2})a^\alpha + A_\epsilon}{Laa^\alpha} = \frac{b}{La} + \frac{1}{2} + \frac{A_\epsilon}{Laa^\alpha} > \frac{1}{2}.$$

Case 3. $c < \frac{aL}{2} \leq 2c - b$. The filter response $|f * \phi_{a,\theta}(p)|$ is still minimal when $\theta = \pi/2$ while the maximal response occurs for an angle $0 \leq \bar{\theta} < \pi/2$.

We consider first the case where $\bar{\theta} = 0$. Denoting by A_δ the area of region of intersection of the rectangle $Q_{a,0}$ and the disk S for $x > c$ (see Fig. 1(b)) we have

$$D_a f(p) = \frac{(b + \frac{aL}{2})a^\alpha + A_\epsilon}{2ca^\alpha + 2A_\delta}.$$

Next we observe that $A_\delta < \delta a^\alpha$, where $\delta = \sqrt{R^2 - (y - \frac{a^\alpha}{2})} - \sqrt{R^2 - (y + \frac{a^\alpha}{2})}$. We can estimate δ as

$$\delta \leq \frac{2ya^\alpha}{\sqrt{R^2 - (y - \frac{a^\alpha}{2})} + \sqrt{R^2 - (y + \frac{a^\alpha}{2})}} \leq \frac{2ya^\alpha}{2\sqrt{R^2 - (y + \frac{a^\alpha}{2})}} = \frac{ya^\alpha}{c}.$$

From the last observation, using the fact that $b > a^\alpha$ and $2c < aL$, it follows that

$$D_a f(p) \geq \frac{(b + \frac{aL}{2})a^\alpha}{2ca^\alpha + 2\frac{ya^\alpha}{c}a^\alpha} = \frac{1}{2}\,\frac{2b + aL}{2c + 2\frac{y}{c}a^\alpha} > \frac{1}{2}\,\frac{aL + 2a^\alpha}{aL + 2\frac{y}{c}a^\alpha}. \tag{6}$$

Let $y = \beta R$, with $0 < \beta \leq 1$. Observe that $R^2 = (y + \frac{a^\alpha}{2})^2 + c^2$ so that $c^2 = R^2 - (y + \frac{a^\alpha}{2})^2$. Hence we can write

$$\frac{y^2}{c^2} = \frac{\beta^2 R^2}{(1 - \beta^2)R^2 - \beta R a^\alpha - \frac{a^{2\alpha}}{4}} \leq \frac{\beta^2 R^2}{(1 - \beta^2)R^2 - \frac{\beta}{5}R^2 - \frac{1}{100}R^2} = \frac{\beta^2}{\frac{99}{100} - \beta^2 - \frac{\beta}{5}}.$$

The above quantity is less than one if $\beta < 0.65$. Hence, using the observation that $\frac{y}{c} < 1$ in (7), it follows that $D_a f(p) > \frac{1}{2}$.

If $\bar{\theta} \neq 0$, then either the rectangle $Q_{a,\bar{\theta}}$ overlaps the boundary of the disk at both ends or one of the two ends is fully contained inside the disk. In the first case, the same estimate used in (7) will imply that $D_a f(p) > \frac{1}{2}$. In the second case, we have

$$D_a f(p) = \frac{(b + \frac{aL}{2})a^\alpha + A_\epsilon}{(c' + \frac{aL}{2})a^\alpha + A_{\delta'}},$$

where c' and $A_{\delta'}$ are shown in Fig. 1(b). Since $c' < \frac{aL}{2}$ and $A_{\delta'} \leq A_\delta$, arguing as above we have

$$D_a f(p) \geq \frac{(b + \frac{aL}{2})a^\alpha}{aLa^\alpha + A_\delta} = \frac{1}{2}\frac{2b + aL}{aL + \frac{y}{c}a^\alpha} > \frac{1}{2}\frac{aL + 2a^\alpha}{aL + \frac{y}{c}a^\alpha} > \frac{1}{2}. \tag{7}$$

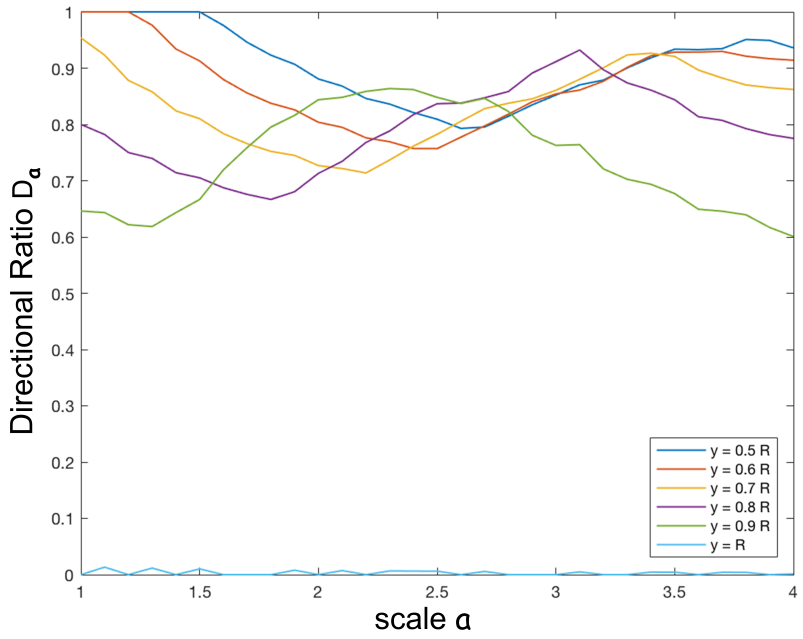

Figure 2: Numerical estimation of the Directional Ratio $D_a f(p)$ as a function of the scale a where f is the characteristic function of a disk of radius R centered at O. We display the result for several locations $p = (0, y)$ where $0.5R \leq y \leq R$. As predicted by Theorem 3, away from the boundary the values of $D_a f(p)$ remain above $\frac{1}{2}$ for a range of scales. To generate this image, we have set $R = 200$ pixels and $L = 130$ pixels. The scale is measured in pixels.

Remark 1. The analysis of part (b) of Theorem 3 can be carried over for larger values of a but the detailed discussion would become very technical. We note that, for 'very large' values of a, approximately if $aL > 4R - 2b$, no rectangles $Q_{a,\theta}$ is contained in S and the directional ratio becomes a constant function of a, namely

$$D_a(p) = \frac{|f * \phi_{a,0}(p)|}{|f * \phi_{a,\pi/2}(p)|} \approx \frac{c}{R}.$$

We also remark that the value of y in the proof of Theorem 3(b) such that $D_a f(p) > \frac{1}{2}$ can be made larger than $0.65R$ even though one cannot get too close to R. If p is selected very close to the boundary of S, the value of $D_a f(p)$ can become very small. Figure 2 displays the values of Directional Ratio computed on a synthetic image $f = \chi_S$ where S is a disk of radius R centered at the origin, as a function of the scale, for representative locations p. The figure shows that the behavior is consistent with the theoretical prediction and that there exists a range of scales such $D_a(p) > \frac{1}{2}$ even for p close to the boundary.

Remark 2. As mentioned above, Theorem 3 is motivated by the problem of separating neurites from somas in microscopy images. Let us be more specific about the dimensions found in typical experimental images.

In a primary rat hippocampal neuron – a frequent animal model – a soma is typically between 10 and 20 μm in diameter, while neurites have diameters between 0.5 and 1.5 μm [19, 20]. Hence in a typical confocal fluorescent image such as Figure 3, where resolution is about 0.25 μm per pixel, a soma is about 40 to 80 pixels in diameter and a neurite is about 2 to 6 pixels in diameter.

Below we verify that the assumptions of Theorem 3 are satisfied in typical images of neurons and show that we can find a range of scales where the computed values of the Directional Ratio separate somas from neurites. For simplicity, we assume that $\alpha = 1/2$.

Based on the dimensions indicated above, we model a neurite as a long rectangle of width $w = 6$. Hence, by choosing $L = 13$ the assumption of Theorem 3(a) is satisfied and $D_a f(p) < 1/2$ for $a > 24/13$. Next we model a soma as a disk S of radius $R = 20$. According to Theorem 3(b), we need to impose $\sqrt{a} \leq \frac{R}{5}$, that is, $a \leq 4$. Hence, for $y = 0.65R$, we find that $b \approx 0.35R$, $c \approx 0.76R$ so that Case 1 holds for $a \leq 1.08$, Case 2 holds for $1.08 < a \leq 2.34$ and Case 3 holds for $2.34 < a \leq 3.60$. For $y = 0.50R$, we find that $b \approx 0.50R$, $c \approx 0.87R$ so that Case 1 holds for $a \leq 1.54$, Case 2 for $1.54 < a \leq 2.68$, Case 3 for $2.68 < a \leq 3.82$.

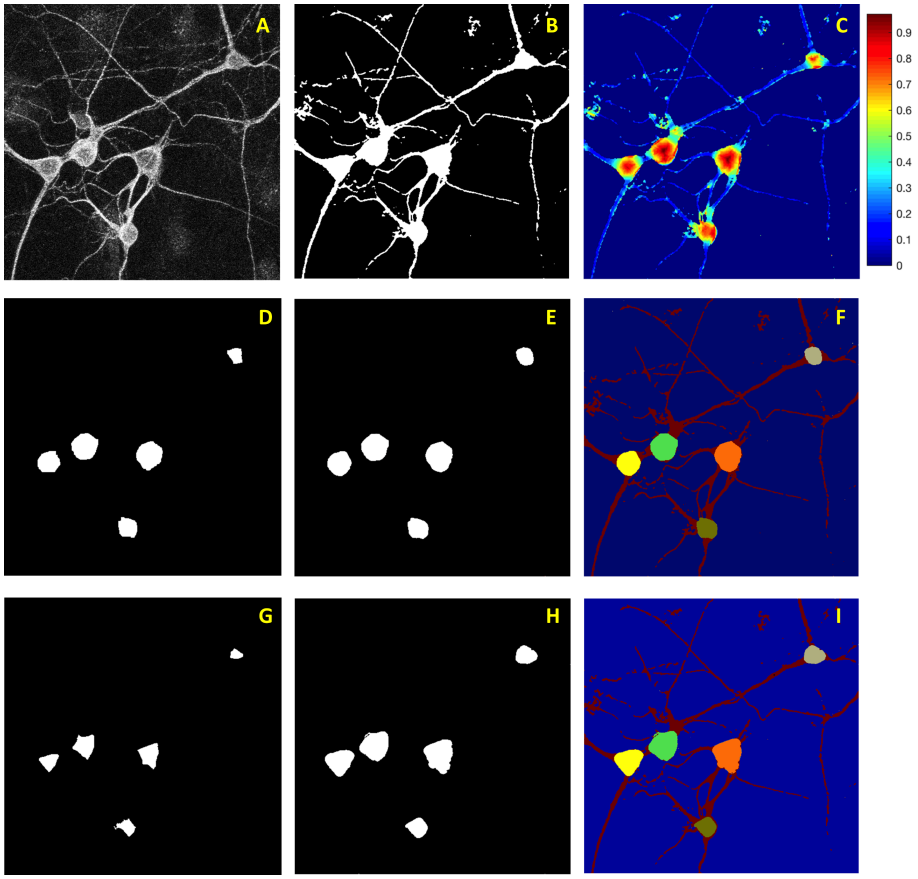

Figure 3: Soma segmentation based on the Directional Ratio. (A) Confocal image of cultured neurons stained with soma-dendritic (MAP2) marker. Image size 512×512 pixels (1 pixel = 0.25 μm) (B) Segmented binary image. (C) Directional Ratio computed inside the segmented region (white region in Panel B). Values range between 0 and 1. For this computation: $a = 2$, $L = 24$. Soma region is obtained by thresholding the Directional Ratio with threshold 0.5 (D) and next applying the Level Set method (E). This computation is repeated by thresholding the Directional Ratio with threshold 0.9 (G) and applying the Level Set method (H). Segmented somas overlapping the segmented image from the two versions of the algorithm are shown in (F) and (I).

3.2. Multiscale anisotropic Gaussian filters

There are other possible choices of directional filters in (5). An important class of examples are the oriented anisotropic Gaussian functions – a class of functions originally introduced for problems of edge detection [21]. They are obtained by scaling a 2D Gaussian using different factors σ_x and σ_y in the x and y directions, respectively, as

$$g_0(x, y; \sigma_x, \sigma_y) = \frac{1}{2\pi\sigma_x\sigma_y} \exp\left(-\frac{1}{2}\left(\frac{x^2}{2\sigma_x^2} + \frac{y^2}{2\sigma_y^2}\right)\right),$$

and next rotating the coordinate axes by an angle θ, obtaining:

$$g_\theta(x, y; \sigma_x, \sigma_y) = \frac{1}{2\pi\sigma_x\sigma_y} \exp\left(-\frac{1}{2}\left(\frac{(x\cos\theta + y\sin\theta)^2}{\sigma_x^2}\,\frac{(-x\sin\theta + y\cos\theta)^2}{\sigma_y^2}\right)\right).$$

One of the most useful properties of these functions is the existence of a very efficient numerical algorithm to implement their convolution in a separable form [22]. That is, the convolution with the anisotropic Gaussian $g_\theta(x, y; \sigma_x, \sigma_y)$ can be expressed as the composition of a 1D convolution with a Gaussian filter in the x direction followed by another 1D convolution with a Gaussian filter in a non-orthogonal direction, namely:

$$g_\theta(x, y; \sigma_x, \sigma_y) = \frac{1}{2\pi\sigma_x\sigma_\phi} \exp\left(-\frac{1}{2}\frac{x^2}{\sigma_x^2}\right) * \exp\left(-\frac{1}{2}\frac{t^2}{\sigma_\phi^2}\right),$$

where $t = x\cos\phi + y\sin\phi$ and ϕ is an appropriate functions of θ. Additionally, one can implement the 1D Gaussian convolutions using a recursive approximation yielding an algorithm that is numerically accurate and faster than a FFT-based 2D convolution, as it requires only $O(1)$ multiplications per pixel. In [16], the authors of this paper have adapted this idea to obtain a very fast algorithm for the computation of the Directional Ratio. In particular, we have shown in [16] that, for a typical image of 512×512 pixels, the computing time of the algorithm for soma detection based on the Directional Ratio is reduced of about a factor of four when the 2D convolution of rectangular filters is replaced by the separable convolution of Gaussian filters going from 0.86s to 0.21s (using a MacBook with Intel Core i5 2.4GHz processor and 16 GB RAM).

3.3. Soma segmentation

As described above, the evaluation of the Directional Ratio of an image is designed to provide quantitative information useful to separate blob-like regions from vessel-like structures. A direct application of this idea to separate somas from neurites in an image of a neurons is illustrated in Fig. 3 and consists of the following steps: (1) the image is segmented (Fig. 3(b)); (2) the Directional Ratio is computed at an appropriate scale using as a mask the segmented image (Fig. 3(c)); (3) by setting a threshold on the Directional ratio plot, two regions are found within the segmented image corresponding to somas and neurites (Fig. 3(d)). As the figure shows, the method based on the Directional Ratio works rather well. This implementation has however some limitations due to the simplifying assumptions of our model. In experimental images, somas are not circular but may be elongated with irregular boundaries. In addition, our model did not consider that somas and neurites do intersect. To improve the algorithm, a relatively simple refinement is also illustrated in Fig. 3 and consists in the following steps: after computing the Directional Ratio on the segmented image, the threshold is set at a higher value resulting in the detection of a smaller region (Fig. 3(g)) that is successively extended using the classical Level Set algorithm (Fig. 3(h)). The final result displayed in Fig. 3(i) shows that this method accurately segments the somas. A more extensive numerical demonstration of this algorithm including a comparison with competing algorithms can be found in [16]. We remark that the selection of the scale parameter at which to compute the Directional Ratio can be automatized by estimating the 'dominant scale' of the image using the principles of automated scale selection [16, 23].

4. Digital neuron reconstruction

As mentioned above, despite the many initiatives and the significant progress made by the scientific community, digital neuron reconstruction remains a challenging problem and existing algorithms have still significant limitations. In particular, most methods are still focused on single-neuron reconstruction. Even

though there are tracing algorithms that perform competitively even on images containing multiple neurons [6, 24, 25] they are not designed to automatically sort traces into neuronal arbors corresponding to individual neurons unless the neurons are well separated in the image [26]. However, even in images of neuronal cultures where cells have low density as in Fig. 3, it is common to have neurites that appear to overlap and cannot be reliably sorted by current tracing algorithms. Removing this limitation is highly desirable in applications of neuronal profiling and high-content screening where it is required to extract multiple characteristics of individual neurons.

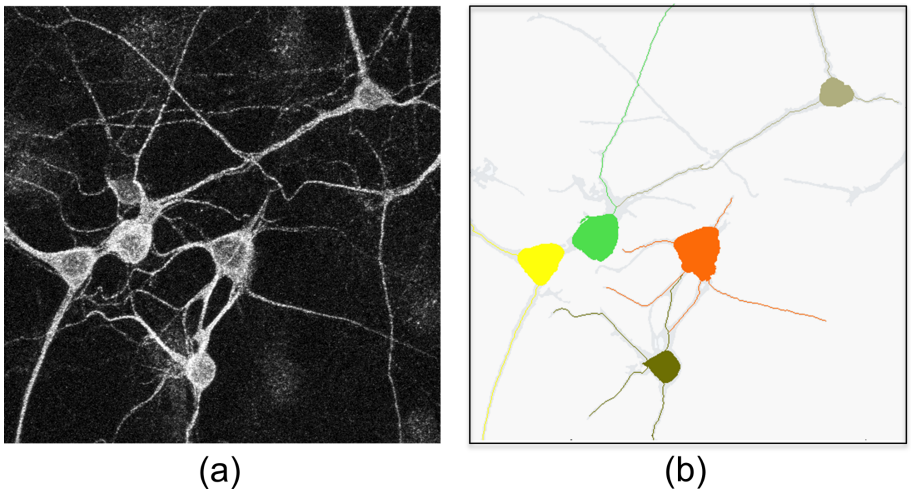

Figure 4: *Neuronal tracing. (a) Confocal image of cultured neurons labelled with anti-MAP2 antibody and (b) corresponding digital reconstruction where somas are segmented and separate individual trees are extracted for each neuron.*

We outline below a strategy for neuronal tracing that is designed to sort individual neuronal trees found in two-dimensional images where neurites from different neurons may overlap. This method is not attempting to trace any possible neurite in the image but only those that can be reliably attributed to a neuron. It relies critically on the soma segmentation method described above to identify each neuron and set the root of each neuronal tree. It consists of the following steps: (i) it preprocesses the image to remove noise and blur; (ii) it

segments the image and separates somas from neurites as described in Sec. 3; (iii) starting from the segmented somas, it compute paths along the neurites emanating from each soma; intersecting neurites are solved by following the path with minimal change in orientation. The application of this method to compute individual trees for each neuron in an image of a neuronal culture is illustrated in Fig. 4.

By computing separate traces for each neuron, this algorithm enables the computation of multiple morphometric characteristics corresponding to each neuron in the image. Additionally, each computed trace provides a local coordinate system to compute local expression levels of analytes visualized in the fluorescent image. The detailed description and illustration of this algorithm goes beyond the scope of this paper and will be discussed in future work.

Acknowledgements

D.L. acknowledges support from GEAR 113491, the Simon foundation (422488) and NSF-DMS 1720487 and 1720452.

References

[1] G. A. Ascoli, D. E. Donohue, M. Halavi, Neuromorpho.org: A central resource for neuronal morphologies, Journal of Neuroscience 27 (35) (2007) 9247–9251. doi:10.1523/JNEUROSCI.2055-07.2007.

[2] K. Brown, G. Barrionuevo, A. Canty, V. Paola, J. Hirsch, G. Jefferis, J. Lu, M. Snippe, I. Sugihara, G. Ascoli, The DIADEM data sets: representative light microscopy images of neuronal morphology to advance automation of digital reconstructions, Neuroinformatics 9 (2-3) (2011) 143–157.

[3] Y. Liu, The DIADEM and beyond, Neuroinformatics 9 (2-3) (2011) 99–102.

[4] R. Parekh, G. A. Ascoli, Neuronal morphology goes digital: a research hub for cellular and system neuroscience, Neuron 77 (6) (2013) 1017–1038. doi:10.1016/j.neuron.2013.03.008.

[5] H. Peng, B. Roysam, G. A. Ascoli, Automated image computing reshapes computational neuroscience, BMC Bioinformatics 14 (1) (2013) 293. doi:10.1186/1471-2105-14-293.

[6] H. Peng, E. Meijering, G. A. Ascoli, From DIADEM to bigneuron, Neuroinformatics 13 (3) (2015) 259–260. doi:10.1007/s12021-015-9270-9.

[7] E. J. Candes, D. L. Donoho, New tight frames of curvelets and optimal representations of objects with piecewise c2 singularities, Communications on Pure and Applied Mathematics 57 (2) (2004) 219–266. doi:10.1002/cpa.10116.

[8] G. Kutyniok, D. Labate, Shearlets: Multiscale Analysis for Multivariate Data, Springer, 2012.

[9] D. Labate, W. Lim, G. Kutyniok, G. Weiss, Sparse multidimensional representation using shearlets, SPIE Proc. 5914, SPIE, Bellingham (2005) 254–262.

[10] K. Guo, D. Labate, The construction of smooth Parseval frames of shearlets., Math. Model. Nat. Phenom. 8 (1) (2013) 82–105. doi:10.1051/mmnp/20138106.

[11] K. Guo, D. Labate, Optimally sparse multidimensional representation using shearlets, SIAM J. Math. Anal. 39 (1) (2007) 298–318.

[12] J. B. Pawley, Handbook of biological confocal microscopy, Springer, New York (N.Y.), 2006.

[13] C. M. Weaver, J. D. Pinezich, W. B. Lindquist, M. E. Vazquez, An algorithm for neurite outgrowth reconstruction., J. Neurosci. Methods 124 (2003) 197–205.

[14] S. C. B. M. W. D. D. S. M. T. S. S. G. J. M. Vallotton P, Lagerstrom R, Automated analysis of neurite branching in cultured cortical neurons using hca-vision., Cytom.Part A 71 (10) (2007) 889–895.

[15] S. K. Schmitz, J. J. Hjorth, R. M. Joemai, R. Wijntjes, S. Eijgenraam, P. de Bruijn, C. Georgiou, A. P. de Jong, A. van Ooyen, M. Verhage, L. N. Cornelisse, R. F. Toonen, W. Veldkamp, Automated analysis of neuronal morphology, synapse number and synaptic recruitment, J Neurosci Methods 195 (2) (2011) 185–193. doi:10.1016/j.jneumeth.2010.12.011.

[16] C. B. Kayasandik, D. Labate, Improved detection of soma location and morphology in fluorescence microscopy images of neurons, Journal of Neuroscience Methods 274 (2016) 61–70. doi:10.1016/j.jneumeth.2016.09.007.

[17] D. Labate, F. Laezza, P. Negi, B. Ozcan, M. Papadakis, Efficient processing of fluorescence images using directional multiscale representations, Math. Model. Nat. Phenom. 9 (5) (2014) 177–193.

[18] B. Ozcan, P. Negi, F. Laezza, M. Papadakis, D. Labate, Automated detection of soma location and morphology in neuronal network cultures, PloS one 10 (4).

[19] N. Bannister, A. Larkman, Dendritic morphology of ca1 pyramidal neurones from the rat hippocampus: I. branching patterns, Journal of Comparative Neurology 360 (1) (1995) 150–160.

[20] J. C. Fiala, K. M. Harris, K. Spacek, Dendrite structure, Oxford University Press Oxford (UK), 1999.

[21] P. Perona, Steerable-scalable kernels for edge detection and junction analysis, Image Vision Comput. 10 (10) (1992) 663–672.

[22] J.-M. Geusebroek, A. Smeulders, J. van de Weijer, Fast anisotropic gauss filtering, IEEE Trans Image Process 12 (8) (2003) 938–943.

[23] T. Lindeberg, Feature detection with automatic scale selection, International Journal of Computer Vision 30 (2) (1998) 79–116.

[24] D. Jimenez, D. Labate, I. A. Kakadiaris, M. Papadakis, Improved automatic centerline tracing for dendritic and axonal structures, Neuroinformatics 13 (2014) 1–18. doi:10.1007/s12021-014-9256-z.

[25] P. C. S. W. T. J. e. a. Al-Kofahi Y, Dowell-Mesfin D, Improved detection of branching points in algorithms for automated neuron tracing from 3D confocal images., Cytom.Part A 73(1) (2008) 3643.

[26] P. Vallotton, R. Lagerstrom, C. Sun, M. Buckley, D. Wang, et al., Automated Analysis of Neurite Branching in Cultured Cortical Neurons Using HCA-Vision., Cytom. Part A 71 (10) (2007) 889–895.